Significant Phonon Chirality Activated by Crystalline Electric Field Excitations in $KNdSe_2$

Zheng Zhang,[1] Yanzhen Cai,[1,2] Mingtai Xie,[1,2] Helin Mei,[2] Weizhen Zhuo,[1,2] Jianting Ji,[1] Feng Jin,[1] and Qingming Zhang[1,2,*]

[1]*Beijing National Laboratory for Condensed Matter Physics, Institute of Physics, Chinese Academy of Sciences, Beijing 100190, China*
[2]*School of Physical Science and Technology, Lanzhou University, Lanzhou 730000, China*

(Received 27 October 2025; revised 10 April 2026; accepted 28 April 2026; published 21 May 2026)

Chiral phonons, lattice vibrations carrying finite angular momentum, are at the forefront of a fast-developing field for exploring and controlling quantum materials in captivating ways. Phonon chirality originating from topological phonon bands is physically interesting but generally small and limited to a few material classes. Here, we report the observation of significant phonon chirality in the triangular-lattice rare-earth compound $KNdSe_2$. We find that the chirality is activated by a distinct local mechanism—crystalline electric field (CEF) excitations—rather than by a global topology. Using helicity-resolved magneto-Raman spectroscopy, we observe a clear splitting (~ 3 cm^{-1} under 9 T, or equivalently $\sim 0.4\mu_B$) of the degenerate E_g phonon mode that exhibits perfect circular polarization selection rules—the unambiguous fingerprint of chirality. The magnitude, field dependence, and thermal evolution of the splitting are quantitatively reproduced by a microscopic theory of CEF-phonon coupling, which we solve by employing the Dyson equation formalism and incorporating a careful analysis of symmetry and angular momentum conservation. Our findings demonstrate a deterministic, CEF-activated mechanism for realizing phononic chirality and identify the rare-earth chalcogenides as a highly tunable playground for investigating the rich physics of coupled electronic and vibrational quasiparticles.

DOI: 10.1103/frn1-f3t9

Introduction—Chirality, the breaking of mirror symmetry, is a pervasive theme across physics, ranging from the parity violation in elementary particles to the handedness of biomolecules. In the realm of condensed matter, chiral excitations have emerged as a frontier of exploration. Within this domain, chiral phononic excitations [1–4] are of particular interest due to their critical importance in both fundamental physics [5–9] and emerging spintronic applications [3,10–18].

From a general perspective, chiral or topological excitations in different degrees of freedom are often intertwined due to their mutual coupling. A prominent example is found in magnetic skyrmions [19–21], which exhibit intrinsic topological orbital moments (TOM) [22–24] arising from the dynamics of itinerant electrons. Through electron-lattice coupling, these electronic TOMs induce dynamical fluctuations with chiral degrees of freedom spreading over a large number of unit cells. This phenomenon can be regarded as a prototype of chiral phononic excitations; however, it typically yields subtle or weak phonon chirality, as spatial delocalization dilutes the angular momentum transfer, resulting in quasilinear rather than circular atomic motion within any single unit cell.

When the spatial scope is restricted to a single unit cell, atomic movements naturally correspond to standard lattice vibrations, i.e., phonon modes at the Γ point. The widely studied phonon chirality arising from phonon band topology or Berry curvature in reciprocal space is observable yet typically small [1,25,26]. In intrinsic chiral crystals (e.g., quartz, WSe_2), where chirality stems from broken inversion symmetry with intrinsic topological character [27–29], the phonon magnetic moments originate solely from the helical motion of ions and are therefore inherently minute ($\sim\mu_N$) due to the large ionic mass [29]. In systems without spontaneous inversion symmetry breaking, a doubly degenerate phonon mode at the Γ point, such as the E_g mode, can generally be decomposed into left- and right-handed vibrations. In principle, an external magnetic field can lift this degeneracy, enabling the direct observation of a chiral phonon mode. However, in practice, the induced chirality is often subtle and challenging to detect.

Despite this typically weak phonon chirality, effective angular momentum transfer mediated by phonon coupling can fundamentally alter the scenario, yielding a "significant" or "strong" phonon chirality. Therefore, the common ground bridging the "weak" and strong regimes lies in the efficiency of angular momentum transfer to the lattice, which is governed by the spatial overlap between the electronic angular momentum source and the phonon

*Contact author: qmzhang@iphy.ac.cn

coordinate: delocalized sources dilute the transfer over many unit cells, producing weak chirality, whereas localized sources concentrated within a single unit cell enable maximally efficient transfer and giant chirality.

We identify the coupling between local crystalline electric field (CEF) excitations and lattice vibrations in rare-earth materials as a highly effective pathway to realize chiral phonons [30–32]. Spatially, both CEF excitations and Γ-point phonons are characterized by localized intra-unit-cell dynamics, offering a crucial basis for strong, symmetry-protected coupling. Energetically, CEF excitations naturally lie in the range of tens to hundreds of cm^{-1}, overlapping perfectly with the energy scale of Raman-active optical phonons to facilitate resonant coupling. Regarding angular momentum, discrete CEF transitions involve well-defined changes in total angular momentum (ΔJ_z) that can effectively transfer the specific angular momentum required to excite chiral phonon modes. This "triple matching" implies that CEF excitations in rare-earth materials can effectively "activate" significant phonon chirality, potentially leading to the formation of vibronic bound states when the CEF and phonon energies are nearly degenerate [33–36]. The rare-earth chalcogenides [37,38], $ARECh_2$ (where A is an alkali metal, RE is a rare earth, and Ch is a chalcogen), constitute a vast family of magnetic materials that fully satisfy these criteria. Consequently, they emerge as an ideal platform for exploring the coupling between CEF states and chiral lattice dynamics.

Here, we select $KNdSe_2$ as an ideal archetype from this family to investigate CEF-phonon coupling. This compound features a perfect triangular lattice of Nd^{3+} Kramers ions embedded in a D_{3d} symmetric environment, providing a clean and well-defined system. Using high-resolution, circularly polarized magneto-Raman spectroscopy, we report the unambiguous observation of giant chiral phonons activated by the CEF excitations. A clear splitting of the in-plane E_g phonon mode is observed under a magnetic field, exhibiting near-perfect selection rules that directly correspond to left- and right-handed phonon chirality. By solving the Dyson equation [32,39] for a microscopic model of CEF-phonon coupling that includes the full Nd^{3+} CEF scheme, our model shows excellent quantitative agreement with our experimental results. These findings not only present the first observation of chiral phonons in $KNdSe_2$ but also establish the rare-earth chalcogenides as a rich and highly tunable platform for activating, manipulating, and exploring the fundamental physics of chiral and coupled quasiparticles.

Lattice vibrations of $KNdSe_2$—$KNdSe_2$ crystallizes in the rhombohedral space group $R\bar{3}m$ (point group D_{3d}), with magnetic Nd^{3+} ions forming a perfect triangular lattice [Fig. 1(a)]. Temperature-dependent Raman spectra [Fig. 1(c)] reveal two prominent phonon modes at ∼129 and ∼158 cm^{-1}, assigned to the in-plane doubly degenerate E_g and the out-of-plane A_{1g} symmetries, respectively,

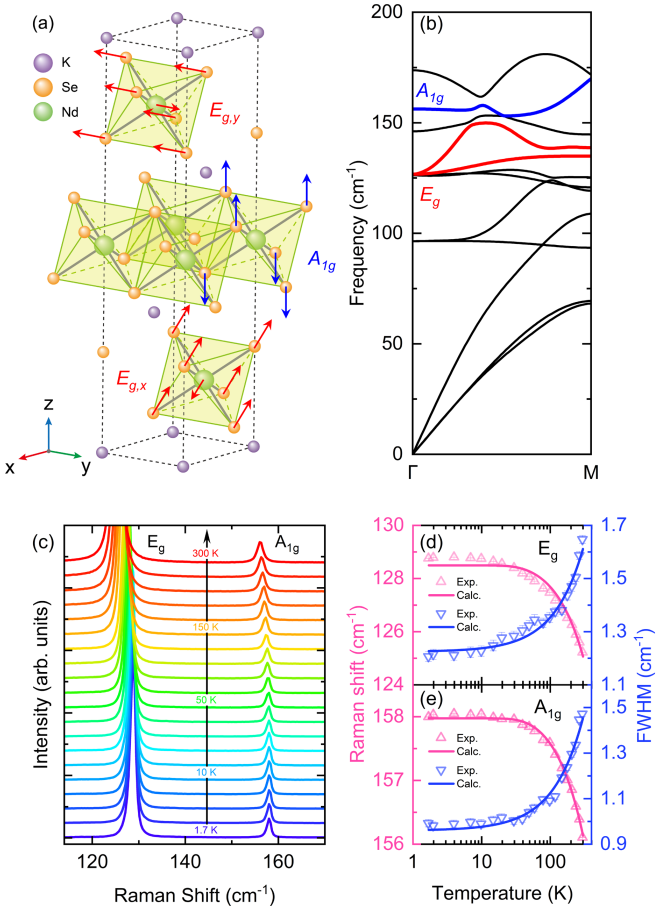

FIG. 1. Lattice dynamics of $KNdSe_2$. (a) Displacement vectors for Raman-active E_g and A_{1g} modes. (b) Phonon dispersion showing E_g (red) and A_{1g} (blue) branches. (c) Temperature-dependent Raman spectra. Frequency and FWHM vs temperature for (d) E_g and (e) A_{1g} modes. Lines indicate anharmonic decay fits.

consistent with first-principles phonon calculations [Fig. 1(b)] [40–44]. Both modes exhibit conventional anharmonic behavior with increasing temperature [Figs. 1(d) and 1(e)]. Beyond lattice dynamics, our Raman spectra reveal sharp electronic transitions associated with CEF excitations of the Nd^{3+} ground-state multiplet.

CEF excitations of $KNdSe_2$—The Nd^{3+} ion ($[Xe]4f^3$, $^4I_{9/2}$ ground-state multiplet, $J = 9/2$) is a Kramers ion, retaining at least double degeneracy in all CEF levels due to time-reversal symmetry. In the D_{3d} environment of $KNdSe_2$, the $^4I_{9/2}$ multiplet splits into five Kramers doublets, described by the CEF Hamiltonian

$$\hat{H}_{\mathrm{CEF}} = \sum_i B_2^0\hat{O}_2^0 + B_4^0\hat{O}_4^0 + B_4^3\hat{O}_4^3 + B_6^0\hat{O}_6^0 + B_6^3\hat{O}_6^3 + B_6^6\hat{O}_6^6, \quad (1)$$

where B_m^n are CEF parameters and $\hat{O}_m^n$ are Stevens operators constructed from $\hat{J}$.

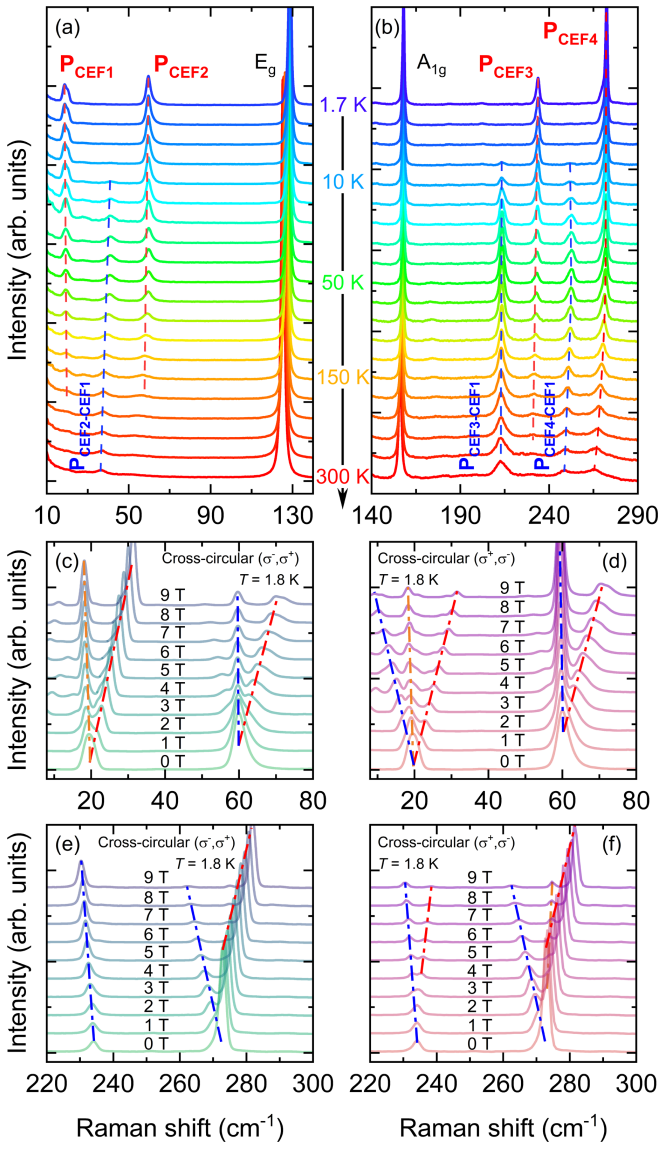

FIG. 2. Temperature and magnetic field evolution of CEF excitations in $KNdSe_2$. (a),(b) Raman spectra (1.7–300 K) identifying four CEF transitions (P_{CEF1}–P_{CEF4}) and phonon modes. (c),(d) Low-energy and (e),(f) high-energy CEF spectra under magnetic fields at 1.8 K in cross-circular polarizations ($\sigma^{\mp},\sigma^{\pm}$).

Temperature-dependent Raman spectra [Figs. 2(a) and 2(b)] reveal, in addition to phonons, seven sharp CEF excitations—four ground-state transitions persisting to 1.7 K and three thermally activated modes vanishing below 10 K—unambiguously identified by their absence in non-magnetic $KLaSe_2$ [45]. To uniquely constrain the CEF Hamiltonian, we also employed polarization-resolved magneto-Raman spectroscopy [Figs. 2(c)–2(f)], fitting ten distinct field-evolving transitions to extract a robust set of B_m^n parameters [45]. The resulting model accurately reproduces the experimental Zeeman splittings (see End Matter) and polarization selection rules, establishing the complete electronic structure of Nd^{3+} in $KNdSe_2$.

Chiral phonon and CEF-phonon coupling—In addition to Zeeman splitting of the CEF levels from broken time-reversal symmetry, we observe a clear magnetic-field-induced splitting of the E_g phonon in $KNdSe_2$. This effect shows strong circular polarization dependence, revealing a coupling between lattice vibrations and $4f$ electronic degrees of freedom, a mechanism confirmed to be distinct from an intrinsic topological phonon origin (see Supplemental Material [45] for control experiments on non-magnetic $KLaSe_2$). The full magneto-Raman response is shown in Figs. 3(a) and 3(b).

At zero field, the doubly degenerate E_g phonon appears as a single peak near 129 cm^{-1}. Applying a magnetic field along the c axis lifts this degeneracy, yielding a clear splitting into higher- (ω^+) and lower-frequency (ω^-) branches. The two split branches exhibit opposite circular polarization selection rules, a definitive signature of chiral phonons. In the (σ^-,σ^+) configuration [Fig. 3(a)], only the ω^- mode is visible, while ω^+ dominates under the (σ^+,σ^-) configuration [Fig. 3(b)]. Their field-dependent evolution [Fig. 3(c)] reveals an initial linear splitting followed by saturation, reaching a maximum of $\sim$3 cm^{-1} at 9 T. This magnitude is remarkably large compared to conventional non-magnetic chiral crystals—such as quartz, with a predicted moment of only $\sim 0.08\mu_N$ [29]—where phonon Zeeman splittings are typically negligible and spectrally unresolvable. From the low-field slope of the phonon splitting, the effective angular momentum carried by the phonon can be extracted using [32]

$$\mu_{\mathrm{ph}} = \frac{\hbar}{2}\frac{\partial(\omega^+ - \omega^-)}{\partial\mu_0 H}, \tag{2}$$

yielding a value of $\mu_{\mathrm{ph}} = 0.402\mu_B$.

To microscopically account for the observed phonon splitting and chirality, we consider a model incorporating the coupling between the E_g phonons and the CEF states of Nd^{3+} under magnetic field. The total Hamiltonian reads [12]

$$\hat{H} = \hat{H}_{\mathrm{CEF}} + \hat{H}_{\mathrm{ph}} + \hat{H}_B + \hat{H}_{\text{CEF-ph}}, \tag{3}$$

where $\hat{H}_{\mathrm{CEF}}$ is defined in Eq. (1). $\hat{H}_{\mathrm{ph}} = \hbar\omega_{E_g}(\hat{a}_x^\dagger\hat{a}_x + \hat{a}_y^\dagger\hat{a}_y)$ describes the degenerate E_g phonons, and $\hat{H}_B = -g_J\mu_0\mu_B H_z\hat{J}_z$ accounts for Zeeman splitting of the Kramers doublets. The key term is the CEF-phonon coupling, $\hat{H}_{\text{CEF-ph}}$, which primarily involves quadrupolar operators of (x^2-y^2, xy) symmetry, is consistent with the in-plane character of the E_g mode revealed by first-principles calculations. By recombining the $E_{g,x}$ and $E_{g,y}$ phonon modes, the effective coupling Hamiltonian can be simplified into the form [45]

$$\hat{H}_{\text{CEF-ph}} \approx \mathcal{G}_{E_g}\left[\hat{O}_2^2(\hat{a}_{x^2-y^2} + \hat{a}_{x^2-y^2}^\dagger) + \hat{O}_2^{-2}(\hat{a}_{xy} + \hat{a}_{xy}^\dagger)\right], \tag{4}$$

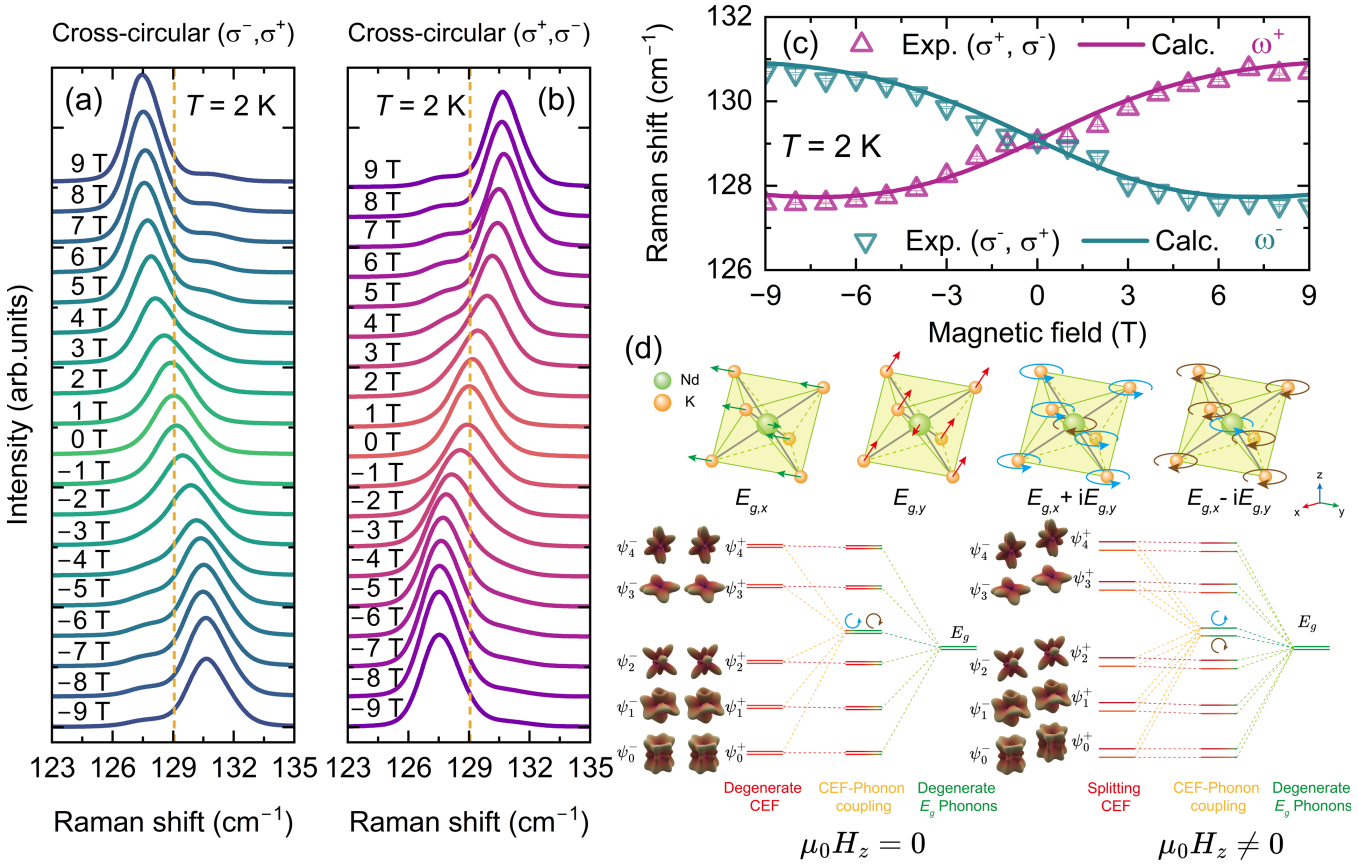

FIG. 3. Magnetic field-induced splitting and chirality of the E_g phonon mode. Field-dependent Raman spectra of the E_g mode at 2 K under (a) (σ^-, σ^+) and (b) (σ^+, σ^-) configurations. Dashed lines indicate the zero-field frequency. (c) Raman shifts of the split branches vs magnetic field. Triangles denote experimental data; solid lines represent calculations using the CEF-phonon coupling model. (d) Microscopic mechanism illustrated with calculated $4f$ electron-cloud distributions for all five Kramers doublets ($\psi_0^{\pm}$ through $\psi_4^{\pm}$). Left ($\mu_0 H_z = 0$): time-reversal symmetry ensures identical electron clouds within each Kramers pair; CEF-phonon coupling yields only a frequency renormalization. Right ($\mu_0 H_z \neq 0$): the Zeeman effect breaks Kramers degeneracy and induces distinct spatial anisotropies in the electron clouds, most prominently for the ground-state doublet. This asymmetry, transferred to the lattice via CEF-phonon coupling, splits the degenerate linear modes ($E_{g,x}, E_{g,y}$) into chiral eigenmodes ($E_{g,x} \pm iE_{g,y}$).

where $\mathcal{G}_{E_g}$ is the coupling strength, and $\hat{O}_{x^2-y^2/xy}$ are Stevens operators (e.g., $\hat{O}_2^{\pm 2}$) reflecting the symmetry of the E_g phonons [45]. The renormalized phonon energies are obtained by solving the Dyson equation for the 2×2 phonon Green's function [32,39], where $\hat{H}_{\text{CEF-ph}}$ contributes the self-energy. As shown by the solid lines in Fig. 3(c), the fitted splitting yields a coupling constant $\mathcal{G}_{E_g} = 2.5$ cm^{-1}. This model quantitatively reproduces the experimental data, capturing both the field-induced splitting and its saturation.

The microscopic origin of the field-induced phonon chirality is illustrated in Fig. 3(d), where the calculated $4f$ electron-cloud distributions for all five Kramers doublets ($\psi_0^{\pm}$ through $\psi_4^{\pm}$) are displayed alongside the CEF energy levels and the E_g phonon. At zero field (left panel), time-reversal symmetry guarantees that each Kramers pair (ψ_i^-, ψ_i^+) exhibits identical electron-cloud shapes. These degenerate Kramers doublets are also related by the mirror symmetry (σ_d) of the D_{3d} point group, which maps the chiral phonon branches $E_g^+ = E_{g,x} + iE_{g,y}$ onto $E_g^- = E_{g,x} - iE_{g,y}$, enforcing their degeneracy. Therefore, CEF-phonon coupling yields only a frequency renormalization without splitting. Dyson equation analysis estimates the bare E_g phonon frequency at ~125.3 cm^{-1}. Applying a magnetic field (right panel) breaks time-reversal symmetry and lifts the Kramers degeneracy via the Zeeman effect. The electron-cloud distributions of the split states develop distinct spatial anisotropies—most prominently for the ground-state doublet ($\psi_0^{\pm}$), as detailed in Supplemental Material Fig. S6 [45]. Crucially, the CEF states are no longer related by the mirror operation, even though the bare E_g phonon modes retain their intrinsic symmetry relationship under σ_d. The E_g^+ and E_g^- branches therefore sense inequivalent electronic environments through the quadrupolar CEF-phonon coupling, producing unequal interaction strengths for the two chiral phonon polarizations. Consequently, the E_g degeneracy is lifted, giving rise to

left- and right-handed chiral phonons $E_g^{\pm} = E_g^x \pm iE_g^y$. This selective coupling is dictated by parity conservation under D_{3d} symmetry. Since the intramultiplet CEF transitions possess even parity ($u \otimes u = g$), they can linearly couple only to even-parity phonons (e.g., Raman-active E_g), while coupling to odd-parity modes (e.g., IR-active E_u) is strictly forbidden.

The emergence of phonon chirality reflects a modified angular momentum conservation law in systems with discrete rotational symmetry. In crystals with threefold (C_3) symmetry, the total angular momentum of the photon-crystal system is conserved modulo $3\hbar$, yielding the selection rule:

$$J_{z,\mathrm{in}} - J_{z,\mathrm{out}} = \Delta J_{z,\mathrm{elec}} + J_{z,\mathrm{ph}} + 3m\hbar, \tag{5}$$

where the angular momentum transferred by light is shared among the CEF excitation, the chiral phonon, and the lattice via angular momentum umklapp ($m = 0, \pm 1$ for E_g modes) [48–50]. While the selection rule outlines allowed outcomes, the dominant quadrupolar CEF-phonon coupling ($\hat{O}_2^{\pm 2}$) favors transitions with $\Delta M_j = \pm 2\hbar$. We consider the (σ^+, σ^-) configuration [Fig. 3(b)], where the light imparts $+2\hbar$ to the system. A self-consistent solution must satisfy both angular momentum conservation and the quadrupolar selection rule. A detailed analysis [45] identifies the dominant channel as an Umklapp process with $m = 1$, involving a favored electronic transition with $\Delta J_{z,\mathrm{elec}} = -2\hbar$. To conserve total angular momentum, $+2\hbar = (-2\hbar)_{\mathrm{elec}} + J_{z,\mathrm{ph}} + 3\hbar$, requiring emission of a left-handed phonon (E_g^+) carrying $+\hbar$. This selective channel, dynamically favored, results in the exclusive observation of the left-handed phonon in this configuration. Conversely, in the (σ^-, σ^+) configuration [Fig. 3(a)], the $-2\hbar$ angular momentum transfer favors a $\Delta J_{z,\mathrm{elec}} = +2\hbar$ transition. Through an umklapp process with $m = -1$, this selectively excites the right-handed phonon (E_g^-) carrying $-\hbar$. This polarization-selective extinction arises from the interplay of angular momentum conservation, operator selection rules, and lattice symmetry—providing unambiguous evidence for the activation of chiral phonons carrying quantized angular momentum.

The essential role of the electronic subsystem in mediating phonon chirality is confirmed by the temperature dependence of the E_g mode splitting (Fig. 4). The field-induced splitting decreases markedly with increasing temperature—dropping from 3.17 cm^{-1} at 2 K to 0.65 cm^{-1} at 15 K—while the polarization selectivity of the split branches weakens, signaling reduced phonon chirality.

This temperature dependence is well captured by our model, where the E_g mode splitting originates from CEF-phonon coupling whose strength reflects the thermal population of Zeeman-split CEF levels. The redistribution across all 10 field-split states follows Boltzmann statistics, $n_i(B,T) = Z^{-1}e^{-E_i(B)/k_BT}$, leading to a reduced effective coupling at elevated temperatures. The underlying physics is captured by a simplified two-level model: for a Zeeman-split

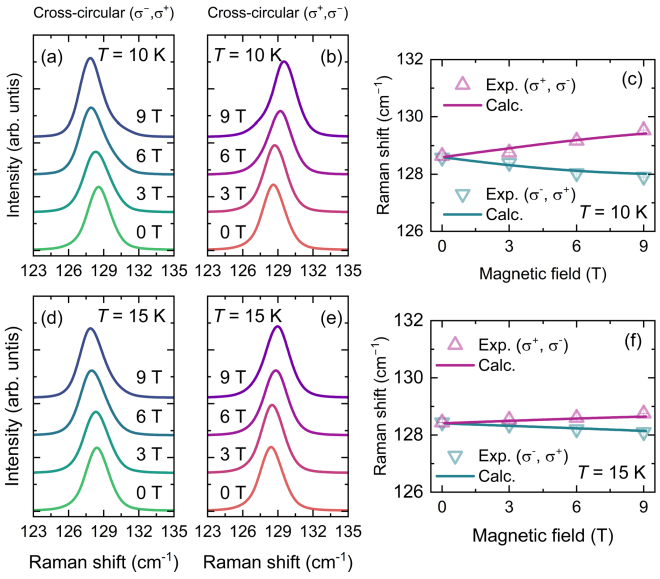

FIG. 4. Temperature dependence of the magnetic-field-induced E_g phonon splitting. (a),(b) Raman spectra at 10 K and (d),(e) at 15 K measured under (σ^-, σ^+) and (σ^+, σ^-) configurations. Raman shifts of the split phonon branches vs magnetic field at (c) 10 and (f) 15 K. Symbols denote experimental data; solid lines represent theoretical calculations.

ground-state doublet, the population imbalance follows $tanh(\delta(H)/2k_BT)$ [32,39]. As temperature increases, thermal fluctuations overcome the Zeeman energy, driving the imbalance toward zero and diminishing the net magnetic polarization. In the full 10-level scheme of Nd^{3+}, elevated temperatures thermally populate higher CEF states, reducing polarization and the population differences relevant to the coupling operator. This suppresses the chiral electronic environment and thus weakens the effective CEF-phonon interaction, leading to reduced phonon splitting. As shown in Figs. 4(c) and 4(e), our calculations incorporating thermal populations accurately reproduce the experimental trends, reinforcing the proposed mechanism.

Summary—The excellent agreement between our comprehensive experimental data and the theoretical model validates this mechanism. Drawing from the physics of CEF-phonon coupling in rare-earth systems, we identify three key ingredients for realizing giant phonon chirality: (i) high lattice symmetry (at least C_3) to support degenerate modes; (ii) strict symmetry and parity matching to ensure active coupling; and (iii) rare-earth ions with large unquenched angular momentum acting as a robust reservoir for efficient angular momentum transfer.

Our findings also enrich the broader understanding of CEF-phonon coupling in f-electron physics. Previous Raman studies have revealed this coupling through scalar observables: summation modes in CeB_6 [51], spectral weight anomalies in $YbRu_2Ge_2$ [52], and vibronic bound states in $TbInO_3$ [53]. Our Letter extends this paradigm to a vector observable—phonon angular momentum—demonstrating

that CEF-phonon coupling not only modifies phonon energies and intensities but also transfers well-defined angular momentum to the lattice via the quadrupolar operators $\hat{O}_2^{\pm 2}$. This connection suggests that helicity-resolved Raman spectroscopy of chiral phonons may serve as a new probe of local multipolar dynamics in correlated f-electron materials. Together with the design principles identified above, our Letter positions the rare-earth chalcogenide family as a versatile platform for exploring magneto-phononic phenomena and coupled quasiparticle physics.

Acknowledgments—This work was supported by the National Key Research and Development Program of China (Grants No. 2024YFA1408300 and No. 2022YFA1402704), the National Science Foundation of China (Grant No. 12274186), the Strategic Priority Research Program of the Chinese Academy of Sciences (Grant No. XDB33010100), the CAS Superconducting Research Project under Grant No. SCZX-0101, the Fund for High-level Talents of Lanzhou and the Synergetic Extreme Condition User Facility (SECUF, [54]).

Data availability— The data are not publicly available. The data are available from the authors upon reasonable request.

[1] Lifa Zhang and Qian Niu, Chiral phonons at high-symmetry points in monolayer hexagonal lattices, Phys. Rev. Lett. **115**, 115502 (2015).
[2] Lifa Zhang and Qian Niu, Angular momentum of phonons and the Einstein–de Haas effect, Phys. Rev. Lett. **112**, 085503 (2014).
[3] Lifa Zhang, Jie Ren, Jian-Sheng Wang, and Baowen Li, Topological nature of the phonon Hall effect, Phys. Rev. Lett. **105**, 225901 (2010).
[4] Hao Chen, Wei Zhang, Qian Niu, and Lifa Zhang, Chiral phonons in two-dimensional materials, 2D Mater. **6**, 012002 (2018).
[5] Tiantian Zhang, Shuichi Murakami, and Hu Miao, Weyl phonons: The connection of topology and chirality, Nat. Commun. **16**, 3560 (2025).
[6] John Bonini, Shang Ren, David Vanderbilt, Massimiliano Stengel, Cyrus E. Dreyer, and Sinisa Coh, Frequency splitting of chiral phonons from broken time-reversal symmetry in CrI_3, Phys. Rev. Lett. **130**, 086701 (2023).
[7] David Lujan, Jeongheon Choe, Swati Chaudhary, Gaihua Ye, Cynthia Nnokwe, Martin Rodriguez-Vega, Jiaming He, Frank Y. Gao, T. Nathan Nunley, Edoardo Baldini, Jianshi Zhou, Gregory A. Fiete, Rui He, and Xiaoqin Li, Spin–orbit exciton–induced phonon chirality in a quantum magnet, Proc. Natl. Acad. Sci. U.S.A. **121**, e2304360121 (2024).
[8] Mengqian Che, Jinxuan Liang, Yunpeng Cui, Hao Li, Bingru Lu, Wenbo Sang, Xiang Li, Xuebin Dong, Le Zhao, Shuai Zhang, Tao Sun, Wanjun Jiang, Enke Liu, Feng Jin, Tiantian Zhang, and Luyi Yang, Magnetic order induced chiral phonons in a ferromagnetic Weyl semimetal, Phys. Rev. Lett. **134**, 196906 (2025).
[9] R. Yang, Y.-Y. Zhu, M. Steigleder, Y.-C. Liu, C.-C. Liu, X.-G. Qiu, T. Zhang, and M. Dressel, Inherent circular dichroism of phonons in magnetic weyl semimetal $Co_3Sn_2S_2$, Phys. Rev. Lett. **134**, 196905 (2025).
[10] Fangliang Wu, Song Bao, Jing Zhou, Yunlong Wang, Jian Sun, Jinsheng Wen, Yuan Wan, and Qi Zhang, Fluctuation-enhanced phonon magnetic moments in a polar antiferromagnet, Nat. Phys. **19**, 1868 (2023).
[11] Fangliang Wu, Jing Zhou, Song Bao, Liangyue Li, Jinsheng Wen, Yuan Wan, and Qi Zhang, Magnetic switching of phonon angular momentum in a ferrimagnetic insulator, Phys. Rev. Lett. **134**, 236701 (2025).
[12] Dominik M. Juraschek, Tomá š Neuman, and Prineha Narang, Giant effective magnetic fields from optically driven chiral phonons in $4f$ paramagnets, Phys. Rev. Res. **4**, 013129 (2022).
[13] Jiaming Luo, Tong Lin, Junjie Zhang, Xiaotong Chen, Elizabeth R. Blackert, Rui Xu, Boris I. Yakobson, and Hanyu Zhu, Large effective magnetic fields from chiral phonons in rare-earth halides, Science **382**, 698 (2023).
[14] C. S. Davies, F. G. N. Fennema, A. Tsukamoto, I. Razdolski, A. V. Kimel, and A. Kirilyuk, Phononic switching of magnetization by the ultrafast Barnett effect, Nature (London) **628**, 540 (2024).
[15] Natalia Shabala and R. Matthias Geilhufe, Phonon inverse Faraday effect from electron-phonon coupling, Phys. Rev. Lett. **133**, 266702 (2024).
[16] Yafei Ren, Mark Rudner, and Di Xiao, Light-driven spontaneous phonon chirality and magnetization in paramagnets, Phys. Rev. Lett. **132**, 096702 (2024).
[17] T. F. Nova, A. Cartella, A. Cantaluppi, M. Först, D. Bossini, R. V. Mikhaylovskiy, A. V. Kimel, R. Merlin, and A. Cavalleri, An effective magnetic field from optically driven phonons, Nat. Phys. **13**, 132 (2017).
[18] Lun-Hui Hu, Jiabin Yu, Ion Garate, and Chao-Xing Liu, Phonon helicity induced by electronic Berry curvature in Dirac materials, Phys. Rev. Lett. **127**, 125901 (2021).
[19] Albert Fert, Nicolas Reyren, and Vincent Cros, Magnetic skyrmions: Advances in physics and potential applications, Nat. Rev. Mater. **2**, 17031 (2017).
[20] Naoto Nagaosa and Yoshinori Tokura, Topological properties and dynamics of magnetic skyrmions, Nat. Nanotechnol. **8**, 899 (2013).
[21] Stefan Heinze, Kirsten Von Bergmann, Matthias Menzel, Jens Brede, André Kubetzka, Roland Wiesendanger, Gustav Bihlmayer, and Stefan Blügel, Spontaneous atomic-scale magnetic skyrmion lattice in two dimensions, Nat. Phys. **7**, 713 (2011).
[22] Manuel Dos Santos Dias, Juba Bouaziz, Mohammed Bouhassoune, Stefan Blügel, and Samir Lounis, Chirality-driven orbital magnetic moments as a new probe for topological magnetic structures, Nat. Commun. **7**, 13613 (2016).
[23] Fabian R. Lux, Frank Freimuth, Stefan Blügel, and Yuriy Mokrousov, Engineering chiral and topological orbital magnetism of domain walls and skyrmions, Commun. Phys. **1**, 60 (2018).
[24] Felix Nickel, André Kubetzka, Mara Gutzeit, Roland Wiesendanger, Kirsten Von Bergmann, and Stefan Heinze,

Antiferromagnetic order of topological orbital moments in atomic-scale skyrmion lattices, npj Spintronics **3**, 7 (2025).
[25] Hanyu Zhu, Jun Yi, Ming-Yang Li, Jun Xiao, Lifa Zhang, Chih-Wen Yang, Robert A. Kaindl, Lain-Jong Li, Yuan Wang, and Xiang Zhang, Observation of chiral phonons, Science **359**, 579 (2018).
[26] Kyosuke Ishito, Huiling Mao, Yusuke Kousaka, Yoshihiko Togawa, Satoshi Iwasaki, Tiantian Zhang, Shuichi Murakami, Jun-ichiro Kishine, and Takuya Satoh, Truly chiral phonons in α-HgS, Nat. Phys. **19**, 35 (2023).
[27] Tiantian Zhang, Zhiheng Huang, Zitian Pan, Luojun Du, Guangyu Zhang, and Shuichi Murakami, Weyl phonons in chiral crystals, Nano Lett. **23**, 7561 (2023).
[28] Kazuki Ohe, Hiroaki Shishido, Masaki Kato, Shoyo Utsumi, Hiroyasu Matsuura, and Yoshihiko Togawa, Chirality-induced selectivity of phonon angular momenta in chiral quartz crystals, Phys. Rev. Lett. **132**, 056302 (2024).
[29] Hiroki Ueda, Mirian García-Fernández, Stefano Agrestini, Carl P. Romao, Jeroen Van Den Brink, Nicola A. Spaldin, Ke-Jin Zhou, and Urs Staub, Chiral phonons in quartz probed by X-rays, Nature (London) **618**, 946 (2023).
[30] G Schaack, Observation of circularly polarized phonon states in an external magnetic field, J. Phys. C **9**, L297 (1976).
[31] G. Schaack, Magnetic field dependent splitting of doubly degenerate phonon states in anhydrous cerium-trichloride, Z. Phys. B Condens. Matter **26**, 49 (1977).
[32] Swati Chaudhary, Dominik M. Juraschek, Martin Rodriguez-Vega, and Gregory A. Fiete, Giant effective magnetic moments of chiral phonons from orbit-lattice coupling, Phys. Rev. B **110**, 094401 (2024).
[33] Zheng Zhang, Xiaoli Ma, Jianshu Li, Guohua Wang, D. T. Adroja, T. P. Perring, Weiwei Liu, Feng Jin, Jianting Ji, Yimeng Wang, Yoshitomo Kamiya, Xiaoqun Wang, Jie Ma, and Qingming Zhang, Crystalline electric field excitations in the quantum spin liquid candidate $NaYbSe_2$, Phys. Rev. B **103**, 035144 (2021).
[34] Enlai Wang, Min Zhang, Chao An, Ying Zhou, Yonghui Zhou, Jian Zhou, and Zhaorong Yang, Crystal electric field excitation and vibrational properties of the quantum spin liquid candidate $LiYbSe_2$, Phys. Rev. B **109**, 174101 (2024).
[35] A. Sethi, J. E. Slimak, T. Kolodiazhnyi, and S. L. Cooper, Emergent Vibronic Excitations in the Magnetodielectric Regime of Ce_2O_3, Phys. Rev. Lett. **122**, 177601 (2019).
[36] Yun-Yi Pai, Claire E. Marvinney, Ganesh Pokharel, Jie Xing, Haoxiang Li, Xun Li, Michael Chilcote, Matthew Brahlek, Lucas Lindsay, Hu Miao, Athena S. Sefat, David Parker, Stephen D. Wilson, Jason S. Gardner, Liangbo Liang, and Benjamin J. Lawrie, Angular-momentum transfer mediated by a vibronic-bound-state, Adv. Sci. **11**, 2304698 (2024).
[37] Weiwei Liu, Zheng Zhang, Jianting Ji, Yixuan Liu, Jianshu Li, Xiaoqun Wang, Hechang Lei, Gang Chen, and Qingming Zhang, Rare-Earth chalcogenides: A large family of triangular lattice spin liquid candidates, Chin. Phys. Lett. **35**, 117501 (2018).
[38] Mingtai Xie, Weizhen Zhuo, Yanzhen Cai, Zheng Zhang, and Qingming Zhang, Rare-Earth chalcogenides: An inspiring playground for exploring frustrated magnetism, Chin. Phys. Lett. **41**, 117505 (2024).
[39] Peter Thalmeier and Peter Fulde, Optical phonons of rare-earth halides in a magnetic field, Z. Phys. B Condens. Matter **26**, 323 (1977).
[40] G. Kresse and J. Hafner, Ab initio molecular dynamics for liquid metals, Phys. Rev. B **47**, 558 (1993).
[41] G. Kresse and J. Furthmüller, Efficient iterative schemes for ab initio total-energy calculations using a plane-wave basis set, Phys. Rev. B **54**, 11169 (1996).
[42] John P. Perdew, Kieron Burke, and Matthias Ernzerhof, Generalized gradient approximation made simple, Phys. Rev. Lett. **77**, 3865 (1996).
[43] Atsushi Togo, Laurent Chaput, Terumasa Tadano, and Isao Tanaka, Implementation strategies in phonopy and phono3py, J. Phys. Condens. Matter **35**, 353001 (2023).
[44] Atsushi Togo, First-principles phonon calculations with phonopy and phono3py, J. Phys. Soc. Jpn. **92**, 012001 (2023).
[45] See Supplemental Material at http://link.aps.org/supplemental/10.1103/frn1-f3t9 for details of sample synthesis, structural characterization, phonon calculations, symmetry analysis, CEF calculations, Raman measurements, and additional theoretical analysis, which includes Refs. [7,39–44,46,47].
[46] Brian H. Toby and Robert B. Von Dreele, GSAS-II: The genesis of a modern open-source all purpose crystallography software package, J. Appl. Crystallogr. **46**, 544 (2013).
[47] Luis Elcoro, Barry Bradlyn, Zhijun Wang, Maia G. Vergniory, Jennifer Cano, Claudia Felser, B. Andrei Bernevig, Danel Orobengoa, Gemma de la Flor, and Mois I. Aroyo, Double crystallographic groups and their representations on the Bilbao Crystallographic Server, J. Appl. Crystallogr. **50**, 1457 (2017).
[48] N. Bloembergen, Conservation laws in nonlinear optics, J. Opt. Soc. Am. **70**, 1429 (1980).
[49] Yuki Tatsumi, Tomoaki Kaneko, and Riichiro Saito, Conservation law of angular momentum in helicity-dependent Raman and Rayleigh scattering, Phys. Rev. B **97**, 195444 (2018).
[50] Tiantian Zhang and Shuichi Murakami, Chiral phonons and pseudoangular momentum in nonsymmorphic systems, Phys. Rev. Res. **4**, L012024 (2022).
[51] Mai Ye, H.-H. Kung, Priscila F. S. Rosa, Eric D. Bauer, Zachary Fisk, and Girsh Blumberg, Raman spectroscopy of f-electron metals: An example of CeB_6, Phys. Rev. Mater. **3**, 065003 (2019).
[52] Mai Ye, E. W. Rosenberg, I. R. Fisher, and G. Blumberg, Lattice dynamics, crystal-field excitations, and quadrupolar fluctuations of $YbRu_2Ge_2$, Phys. Rev. B **99**, 235104 (2019).
[53] Mai Ye, Xianghan Xu, Xiangyue Wang, Jaewook Kim, Sang-Wook Cheong, and Girsh Blumberg, Crystal-field excitations and vibronic modes in the triangular-lattice spin-liquid candidate $TbInO_3$, Phys. Rev. B **104**, 085102 (2021).
[54] https://cstr.cn/31123.02.SECUF.

End Matter

Appendix: Determination of the CEF parameters—Accurate determination of the CEF parameters is a prerequisite for analyzing the CEF-activated phonon chirality; we outline the procedure below, based on the temperature and magnetic-field evolution of the CEF excitations shown in Fig. 5.

Temperature-dependent Raman spectra reveal the CEF level scheme, but ground-state transitions must be distinguished from thermally activated ones: the former persist down to the lowest temperatures, whereas the latter arise from transitions between excited states and are no longer observed at sufficiently low temperatures. The energy of each thermally activated mode equals the difference between two excited levels, providing a stringent internal consistency check. Figure 5(a) shows the four ground-state transitions (CEF1–CEF4), whose frequencies are essentially temperature-independent, and Fig. 5(b) shows the three thermally activated modes, whose energies coincide with the differences CEFi − CEF1$(i > 1)$ extracted from panel (a), confirming the assignment.

More importantly, a magnetic field applied along the c axis lifts the Kramers degeneracy of each doublet, producing ten field-evolving branches observed in cross-circular polarizations. Because the number of independent Zeeman constraints exceeds that of the CEF parameters, a simultaneous fit to all branches determines the CEF Hamiltonian uniquely. As shown in Figs. 5(c) and 5(d), the calculated Zeeman splittings (solid lines) agree excellently with the peak positions extracted from our Raman spectra, demonstrating that the CEF parameters are uniquely and reliably determined.

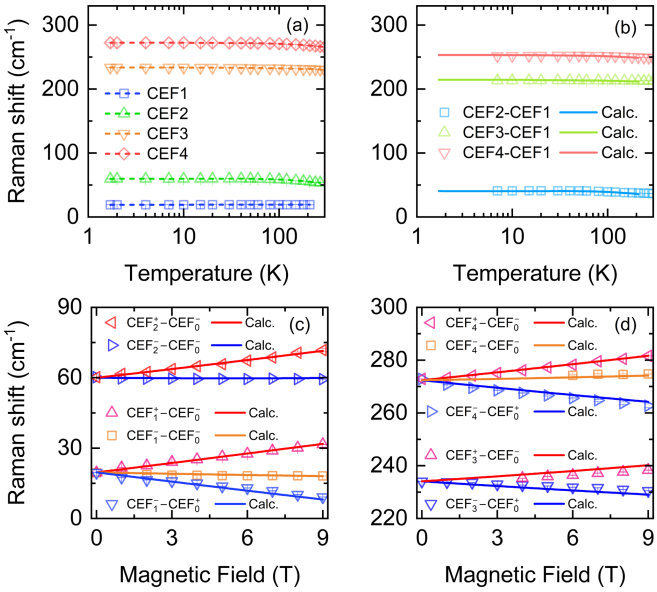

FIG. 5. Temperature and magnetic field evolution of CEF excitations in $KNdSe_2$. (a) Frequencies and (b) energy differences of CEF levels vs temperature. (c),(d) Zeeman splitting of the corresponding CEF levels vs magnetic field. Symbols denote experimental data; solid lines represent CEF calculations.